The Qatar Exoplanet Survey

K. A. A l s u b a i[1], N. R. P a r l e y[2], D. M. B r a m i c h[1], K. H o r n e[2],
A. C o l l i e r C a m e r o n[2], R. G. W e s t[3], P. M. S o r e n s e n[4],
D. P o l l a c c o[5,6], J. C. S m i t h[7] and O. F o r s[1]

[1] Qatar Environment and Energy Research Institute, Qatar Foundation, Tornado Tower,
Floor 19, P.O. Box 5825, Doha, Qatar
e-mail: kalsubai@qf.org.qa
[2] SUPA, School of Physics and Astronomy, University of St Andrews, North Haugh, St
Andrews, Fife, KY16 9SS, UK
[3] Department of Physics and Astronomy, University of Leicester, Leicester, LE1 7RH, UK
[4] Nordic Optical Telescope, Apartado 474, E-38700 Santa Cruz de la Palma, Santa Cruz
de Tenerife, Spain
[5] Department of Physics, University of Warwick, Coventry, CV4 7AL, UK
[6] Astrophysics Research Centre, School of Mathematics and Physics, Queens University,
University Road, Belfast, BT7 1NN, UK
[7] Hidden Loft Observatory, Tucson, AZ 85755, USA

ABSTRACT

The Qatar Exoplanet Survey (QES) is discovering hot Jupiters and aims to discover hot Saturns and hot Neptunes that transit in front of relatively bright host stars. QES currently operates a robotic wide-angle camera system to identify promising transiting exoplanet candidates among which are the confirmed exoplanets Qatar 1b and 2b. This paper describes the first generation QES instrument, observing strategy, data reduction techniques, and follow-up procedures. The QES cameras in New Mexico complement the SuperWASP cameras in the Canary Islands and South Africa, and we have developed tools to enable the QES images and light curves to be archived and analysed using the same methods developed for the SuperWASP datasets. With its larger aperture, finer pixel scale, and comparable field of view, and with plans to deploy similar systems at two further sites, the QES, in collaboration with SuperWASP, should help to speed the discovery of smaller radius planets transiting bright stars in northern skies.

Key words: *Instrumentation: phometers – Surveys – planetary systems*

1. Introduction

The surprising existence of short-period (≈ 4 d) Jupiter-mass extra-solar planets (termed "hot Jupiters"), confirmed by radial velocity measurements in the last decade, has shown us that planetary systems exist in patterns unlike that of our

own Solar System. The class of hot Jupiter planets ($P < 10$ d and $M \sin i < 10 M_J$) makes up $\approx 35\%$ of the planets discovered to date, and $\approx 0.7\%$ of the transiting planets from the Kepler space mission host such a companion (Dong and Zhu 2013). Given a fortuitous geometric alignment, an extra-solar planet may be observed to transit the host star as viewed from the Earth. Such a planetary transit is characterized by a small decrease in the observed brightness of the host star that repeats at the orbital period of the extra-solar planet. The probability that a typical hot Jupiter transits its host star is $\approx 10\%$ (Horne 2003), and hence, being conservative, ≈ 1 in 1400 stars will host a transiting extra-solar hot Jupiter.

Five years after the discovery of the first extra-solar planet around a sun-like star (Mayor and Queloz 1995), the extra-solar planet in orbit around HD 209458 was found to transit the stellar disk (Charbonneau *et al.* 2000, Henry *et al.* 2000). This hot Jupiter was already known to have $M_p \sin i = 0.69 \pm 0.05 M_J$ (M_J is Jupiter's mass, M_p is the planet's mass and i is the orbital inclination) from the radial velocity measurements (Mazeh *et al.* 2000). Also, the spectral type, and hence the mass and radius, of the host star were already known. Consequently, the modeling of the two observed transit events allowed the measurement of the orbital inclination, which in turn allowed the true mass of HD 209458b to be calculated. Charbonneau *et al.* (2000) measured $i = 87°\!.1 \pm 0°\!.2$, implying that $M_p = 0.69 \pm 0.05 M_J$. They also measured $R_p = 1.27 \pm 0.03 R_J$ from the transit fit (where R_p is the planet radius).

The importance of this result lies in the fact that for the first time the mass and radius of an extra-solar planet had been measured, not just a lower limit on the mass. Before this discovery, the radii of the extra-solar planets were unknown and hence their average densities were unknown. The average density derived for HD 209458b was ≈ 0.38 g/cm^3, significantly less than the average density of Saturn (0.7 g/cm^3), the least dense of the Solar System gas giants. This was proof that HD 209458b must be a gas giant rather than a rocky (terrestrial) planet, lending weight to the term hot Jupiter. Average density was not the only important quantity that could be calculated for an extra-solar planet for the first time. Other such quantities included surface gravity and effective temperature.

Since the discovery of the transiting nature of HD 209458b, some 424 transiting planets have been confirmed with periods from 0.18 d to 904 d (see *exoplanet.eu*). This class of extra-solar planet now makes up a significant fraction of the 1047 known extra-solar planets to date. The statistics provided from these systems are helping to pin down the mass–radius relationship for these planets (Fig. 1 reproduced from Chabrier *et al.* 2009). They are also providing a challenge to theories of planetary structure and evolution in order to explain the observed radii (Liu *et al.* 2008), which depend on stellar type, orbital distance, planet mass and age. The results from the modeling of planetary structure have implications for the planetary formation theories, especially in discriminating between the core-accretion model (Ida and Lin 2004) and the gravitational instability scenario (Perryman 2000). The

importance of improving extra-solar planet statistics is paramount for advancing these theories, and for helping to determine the exact definition of what constitutes a planet in the transition regime between brown dwarfs and planets.
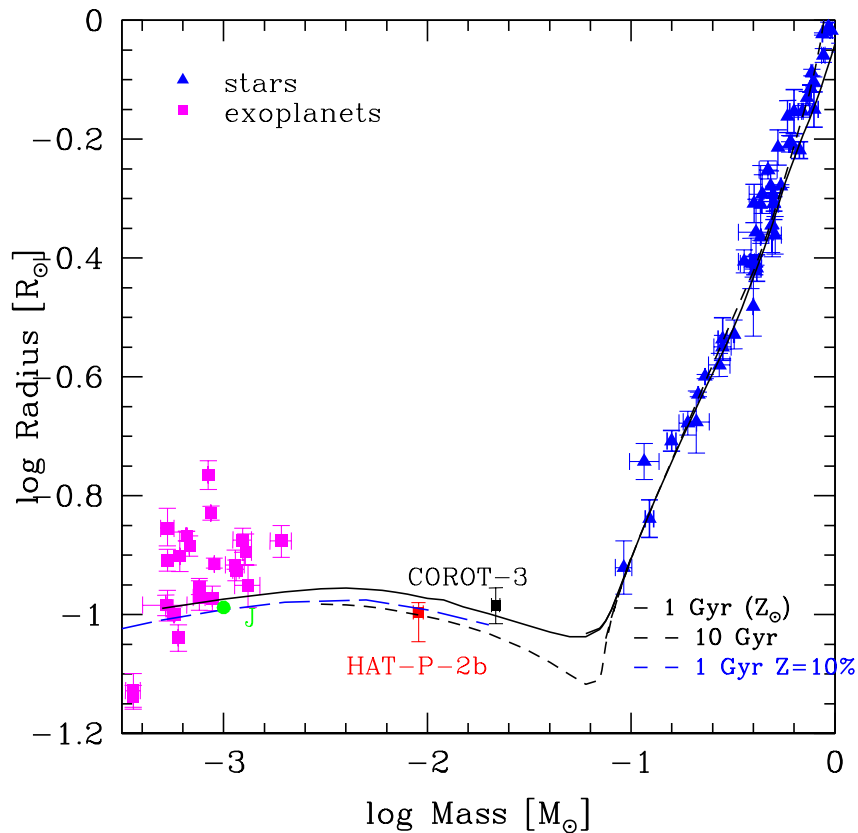

Fig. 1. Mass–radius relationship from the stellar to the planetary regime. The (black) solid and short-dashed lines correspond to models with solar composition, for two isochrones. The long-dashed line corresponds to an object with a $Z = 10\%$ mass fraction of heavy elements. The observationally-determined values of HAT-P-2b and Corot-3b are indicated. Reproduced with permission from Chabrier *et al.* (2009). Copyright 2009, AIP Publishing LLC.

The first major jump in the discoveries of transiting extra-solar planets arrived with the advent of ground-based wide-field surveys of bright stars. Many projects searching for transiting exoplanets have preceded QES. Among those that have met with success are SuperWASP, HAT, XO, TrES and KELT. These pioneering surveys pave the way for new projects such as QES, since they have tackled and solved many hardware and software issues.

A prototypical ground-based exoplanet search project is the Wide-Angle Search for Planets (SuperWASP) survey (Pollacco *et al.* 2006). The SuperWASP survey employs eight camera units attached to a single robotic mount, where each camera uses an E2V 2048×2048 pixel professional CCD backing a 200 mm f/1.8 Canon

lens. Each unit has a field of view (FoV) of 60 square degrees at a scale of $14.''2$ per pixel, giving a field coverage of ≈ 500 square degrees, which is imaged once per minute. SuperWASP targets stars in the brightness regime from 8–13 mag, leading to the discovery of some 80 transiting exoplanets to date.

Currently there is a gap in the magnitude range of stars being surveyed for transiting planets, and this is the range from 12–15 mag where SuperWASP targets become too faint for their instrumentation, and stars are too bright for the deeper surveys, like OGLE (Udalski *et al.* 2002), which start at 15 mag. Exploration of this range is important, because it increases the sampling volume for intrinsically faint K and M-dwarf stars, whose smaller radii facilitate the detection of transits by small planets. QES is designed to fill this gap and detect transiting planets in the range 10–14 mag by constructing survey equipment targeted at this magnitude range.

We are planning to deploy a network of wide-field cameras at three sites around the globe to monitor stars for the presence of transit signals. The first site in New Mexico has been constructed and has been taking data since November 2009. The cameras are wide-field in order to concurrently monitor as many stars as possible. Since a typical hot Jupiter planet has only a $\approx 10\%$ probability of transiting the host star from geometrical considerations, and since it has come to light that $\approx 0.7\%$ of stars host a hot Jupiter, we expect that ≈ 1 in 1400 dwarf stars will show a ≈ 4 d periodic transit signal. In our $5.°3$ FoV, we will be observing anywhere from 10 000 to 50 000 stars simultaneously, the exact number depending on how close we point toward the Galactic plane.

Three QES sites have been chosen strategically to provide better temporal coverage of northern and equatorial stars when combined with the SuperWASP data in future cooperation on chosen fields. The "New Mexico Skies" observing station, located in southern New Mexico at latitude $+32°54'14''$, longitude $105°31'44''$ and elevation 7200 feet, was chosen to complement the SuperWASP-North telescope on La Palma. Our aim is to deploy similar or improved facilities at two additional northern sites at complementary longitudes in order to be able to more rapidly establish ephemerides for transiting exoplanet candidates.

The QES project has developed a customised data pipeline using the DANDIA image subtraction software[1] to process the data and an archive compatible with that of SuperWASP to handle the imaging and light curve datasets necessary for a project with a data rate that is similar to SuperWASP, both outlined in the later sections. We expect ≈ 50 Gb of data per clear night from each site. The data are currently partially processed on site before being fully reduced by the pipeline software system and archived. The pipeline processing has so far been performed at the University of St Andrews while the archive has been hosted at the Universities of Leicester and Warwick. Currently we are moving all processing and archive operations to the Qatar Environment and Energy Research Institute.

---

[1] DANDIA is built from the DANIDL library of IDL routines available at *http://www.danidl.co.uk*

2. The First-Generation QES Wide-Field Camera System

The first QES site, in New Mexico, hosts one wide-field camera system described here and summarized in Table 1. The camera system consists of four 400 mm f/2.8 Canon lenses and one 200 mm f/2.0 Canon lens each with a FLI ProLine PL16801 camera with a $4k \times 4k$-pixel KAF-16801E CCD chip. Each CCD is chilled to a temperature of $-40°$ C to minimize the dark current inherent in such devices. All five cameras are mounted on a Mathis equatorial mount MI-750 (Fig. 2). The 400 mm lenses each have a $5°3 \times 5°3$ FoV, a pixel scale of 4.64 arcsec/pixel and cover the magnitude range from 11–15 by employing an exposure time of 100 s. The 200 mm f/2 lens has an $11° \times 11°$ FoV, a pixel scale of 9.26 arcsec/pixel and covers the magnitude range from 8–12 by employing an exposure time of 60 s. The FoV of the 200 mm lens encapsulates the combined fields of the four 400 mm lenses providing photometry of all stars in the field in the range from 8–15 mag.

T a b l e 1

First-Generation QES Wide-Field Camera System

CCD	5 KAF-16801E-2 , $4k \times 4k$
Lenses	4×400 mm, f/2.8, 1×200 mm, f/2
Mount	Equatorial Fork type mount
FoV	$5°24 \times 5°24$ per CCD for 400 mm lens
Pixel scale	4.64 arcsec/pix for 400 mm lens
Gain	1.7 e^-/ADU
Peak Q.E.	65%
Zero point	1 ADU/s at 23 mag

The focus of the camera lenses is very important for data reduction by difference image analysis (DIA). This is because all DIA algorithms have problems constructing a kernel solution from images with under-sampled PSFs. To investigate the focus effects, different hardware focus setups were used during the first four months of operations. Data taken from 2009 November to 2010 January with the lenses focused provided images with an average FWHM of 1.7 pixels. During 2010 February and March data were taken with the focus set to blur the images to a FWHM of ≈ 3.5 pixels. Comparing the data from the two campaigns showed that the out-of-focus data gave better results than the in-focus data when the out-of-focus data had a FWHM of close to the target value. However, it was found that by de-focusing the lenses the FWHM became very variable and sometimes produced

Fig. 2. The first QES observing station, in New Mexico, is fully functioning. It consists of four 400 mm lenses and one smaller 200 mm lens.

donut-shaped PSFs. As this resulted in poor photometry, we decided to focus the lenses until hardware upgrades could be made to automatically stabilise the out of focus data.

The data acquisition system (DAS), for automatic scheduling and image acquisition, consists of locally networked Windows PC's with one PC assigned to each CCD camera. A master PC provides control of the mount and synchronizes the remaining slave PCs, coordinating slews, focusing, calibration frames as well as when science frames are taken. For example, once a slew is completed as instructed by the master, the master begins its exposure and instructs the slaves to begin theirs.

CCDAUTOPILOT version 4 is a proprietary commercial product that is used extensively by the amateur astronomy community. It is not open source. It was modified by the author (Smith) to provide continuous operation, master/slave control of the multiple systems, coordinated data and calibration frames including sky flats, simultaneous focusing and appropriate file and folder naming for compatibility with SuperWASP. It acts as an executive program controlling other programs for mount slewing, camera operation and focusing *via* the WINDOWS ACTIVEX interface. Other software used is THESKY6 by Software Bisque for telescope control, MAXIM DL by Diffraction Ltd for camera control, FOCUSMAX by Larry Weber and Steve Brady for focusing, and PINPOINT by DC-3 Dreams for plate solving and WCS insertion. An instance of CCDAUTOPILOT runs on each PC and has been modified to run continuously, night after night, without operator intervention

as well as for compatibility with the pipeline-processing program. The software handles weather interrupts by idling the system until the weather clears. If the dome is closed due to adverse weather, the system continues to idle so that it can continue data acquisition once the weather clears and the dome is opened.

For certain session phases, the slaves are autonomous. For example, when sky flats are initiated, all systems determine their own exposures to achieve the targeted signal level *via* an automatic exposure routine. In a similar manner the desired number of dark and bias frames are acquired. When it is desired to update the focus, each system is instructed to run an automatic focus routine. After an activity is instructed to begin, all systems report back when they have completed that activity. When all have reported an idle condition, the systems are instructed to begin the next activity.

The target list is specified by a simple text file and is defined for the year. Another simple text file defines the base exposure time and cooling temperature for each camera. These text files can be accessed by non-Windows PC's, thus not requiring direct access to the DAS. Each evening the software determines the target to be used, based on its elevation and proximity to the moon. When that target sinks to a specified elevation in the West, another target is chosen by the same selection process. WCS coordinates are inserted into the FITS header of the science frames at the end of the evening's session and the data are subsequently presented for transfer by the pipeline.

3. QES Observing Strategy

A full field is defined as a 2×2 mosaic of four sub-fields, numbered 1, 2, 3 and 4 (Fig. 3). Each sub-field is covered by the FoV of one of the four 400 mm lenses, and all four are covered by the encompassing FoV of the 200 mm lens. While the 400 mm cameras take synchronized 100 s exposures, the 200 mm camera takes a 60 s exposure. With these exposure times the 200 mm lens records brighter stars from 9 to 12.5 visual magnitude with an RMS accuracy of 1%, while the 400 mm lenses reach deeper to fainter stars from 10 to 13.75 visual magnitude.

During readout of the CCD images from the 400 mm cameras, the mount slews from pointing A to B (Fig. 3). Once there, the 400 mm cameras again take 100 s exposures while the 200 mm camera takes a 60 s exposure. The slew and exposure sequence then repeats, moving from pointing B to C, and then to pointing D. This full cycle of four pointings takes approximately 8 minutes to complete, including the 20 s CCD readout times. Faint stars in the 12–15 mag range have a photometric measurement from the 400 mm camera system, brighter 8–10 mag stars have a photometric measurement from the 200 mm camera, and stars in the intermediate range 11–12 mag are recorded by both the 200 mm and 400 mm cameras. Thus every 8 minutes a sky area of ≈ 400 square degrees is recorded by both the 200 mm and 400 mm cameras.
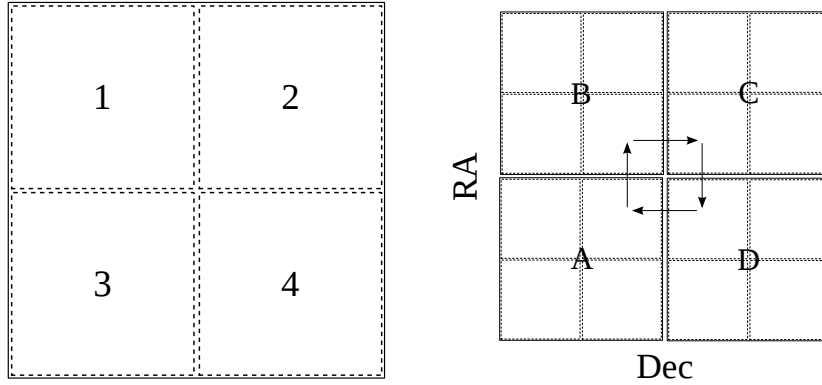
Fig. 3. The $5°3 \times 5°3$ fields of view of the 400 mm lenses are delineated by the smaller boxes (dotted squares) labelled 1 through 4. The $11° \times 11°$ field of view of the 200 mm lens is delineated by the larger enclosing box (solid square). The whole system moves from pointing A to pointing D continuously all night to cover in total ≈ 400 square degrees.

The cycle of measurements is repeated at an observing site throughout the night so long as the chosen field remains higher than 30 degrees above the horizon, below which the airmass is too high for reliable wide-field photometry. A field setting at one site can be picked up by the next site to the West, providing a capability for continuous coverage of the field apart from occasional breaks due to bad weather. As we are aiming to capture the transits of planets with periods from $\approx 0.5-10$ d, we observe each field for a period of two months before moving to the next field. In one year, we can cover up to ten fields.

4. QES Data Reduction

We employ difference image analysis based on the DANDIA software to achieve optimal extraction of light curves from the QES images. The pipeline has a control program to make it fully automatic. The difference image analysis procedure begins by selecting the sharpest (best seeing) image as the reference image. Constraints are imposed on sky background and sky transparency to prevent selecting a reference image with a sharp focus but poor signal-to-noise ratio due to thin cloud and/or bright moon-lit sky background. For each detected star, the flux measured on the reference image (referred to as the reference flux, f_0) is found by optimal scaling of the star's point-spread function (PSF) to fit the reference image data in a pixel box centered on the star's position. The PSF varies considerably over the wide field of the QES images, and we account for this by using a spatially-variable empirical point spread function (PSF) model fitted to all of the detected PSF-like images. Deblending of very close objects is attempted. Stars are matched between each image in the sequence and the reference image, and a linear coordinate transformation is derived and used to resample the images to register them with the star positions on the reference image.

As mentioned in Section 2, in-focus QES images have an under-sampled PSF and yield poor difference image results. We find that DANDIA gives better photometry on these under-sampled images if we first convolve the reference and registered images with a Gaussian function that blurs the star images into adjacent pixels. Fig. 4 shows how the Gaussian function's full-width at half-maximum (FWHM) affects the light curve RMS for stars in different magnitude bins. From Fig. 4 we see that the best results arise after blurring the images with a FWHM between 1.5 and 2.5 pixels. Based on these results, we keep the QES cameras in focus, but blur the reference and registered images by a Gaussian FWHM of 2.5 pixels before performing image subtraction.
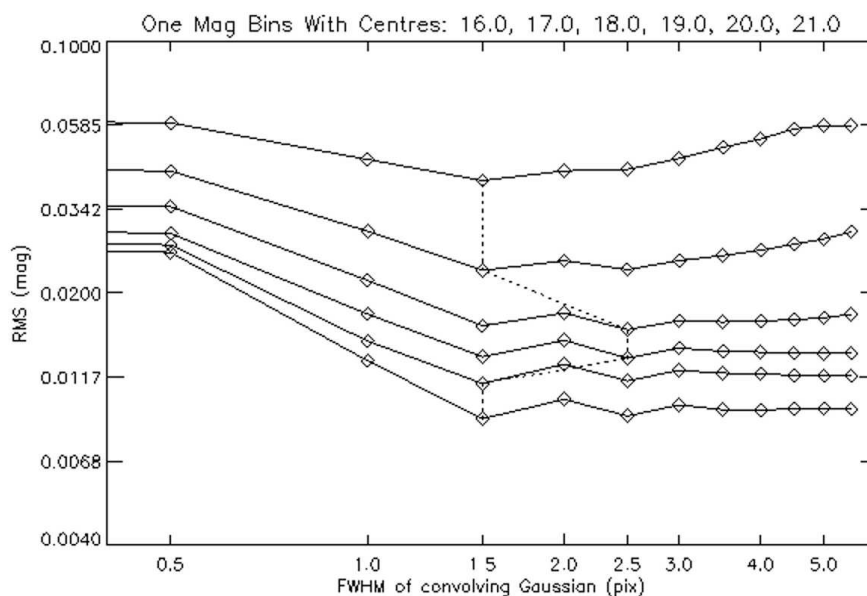

Fig. 4. The effect of different convolving Gaussians used to blur in-focus images, with FWHM of ≈ 1.7 pixels, on the light curve RMS scatter once the data has been processed by difference image analysis. The effect of the different Gaussian blurs for six different instrumental magnitude bins corresponding roughly to *V* mag 11, 12, 13, 14, 15 and 16 respectively is shown.

Image subtraction is preformed using the methods from Bramich (2008). We sub-divide the images into a 14×14 grid of cells and determine for each cell a kernel function, modeled as a pixel array, derived by matching the PSF in each cell of the reference image with the PSF in the corresponding cell of the registered image. The kernel function for each image pixel is obtained by bi-linear interpolation in the grid of kernels. The reference image, convolved with the appropriate kernel function is then subtracted from each registered image to produce a sequence of difference images.

The differential flux, Δf, for each star detected in the reference image is measured on each difference image as follows. The empirical PSF at the measured position of the star on the reference image is determined by shifting the empirical

PSF model corresponding to the nearest pixel by the appropriate sub-pixel shift using image resampling. The empirical PSF model is then convolved with the kernel model corresponding to the star position on the difference image. Finally, the PSF is optimally scaled to fit the difference image at the star position using pixel variances following a standard CCD noise model.

As the reference image is convolved and scaled to match the registered image, the flux change Δf needs to be scaled by the photometric scale factor p derived from the image subtraction kernels as described in Bramich (2008). To correct for partial cloud cover and transparency variations across the large field of view of the lenses, the photometric scale factor is allowed to be spatially variable. This helps improve the light curve quality achieved by better modeling the poorer quality data (Bramich *et al.* 2013). The photometric scale factor is therefore solved for in each grid cell, and interpolated in the same way as the kernel and the differential background.

Light curves for each star are constructed by calculating the total flux $f(t) = f_0 + \Delta f(t)/p(t)$ at time t as the sum of the reference flux f_0 and the time-dependent difference flux $\Delta f(t)$, corrected by the time-dependent (and spatially variable) photometric scale factor $p(t)$. Fluxes are then converted to instrumental magnitudes *via* the standard formula $m = 25 - 2.5\log(f)$, where m is magnitude and f is flux (ADU/s).

To reduce the number of faint stars with a signal-to-noise ratio too low for exoplanet detection, the stars detected by the pipeline are matched with the UCAC3 catalogue (Zacharias *et al.* 2010) and any objects that lack a matching UCAC3 star are not passed to the archive. A magnitude zero point correction is also performed between the reference magnitudes and the UCAC3 magnitudes for all the stars in a given field using a global SVD fit. The resulting absolute photometric correction has a mean RMS scatter of approximately 0.1 mag.

For the first week of observations of any field, the images are simply calibrated for the standard bias, dark and flat field corrections. At the end of the first seven nights of clear weather, the best seeing image with an acceptable sky background is automatically chosen by the software as the reference image. The best seeing image is required since this image will be convolution matched to every other image. The pipeline then produces differential photometry *via* difference image analysis as described above for all images to date, and on a nightly basis for all subsequent observations. The results of the reductions are automatically uploaded for ingestion into the database archive.

5. QES Analysis Strategy and Archive

The reduced photometric data are stored in a data archive system based on that developed for SuperWASP and described in detail by Pollacco *et al.* (2006). The data from each of the survey fields are treated to remove trends due to instrumental systematic errors using the SYSREM algorithm (Tamuz, Mazeh and Zucker 2005,

Collier Cameron *et al.* 2006) and the Trend Filtering Algorithm (Kovács, Bakos and Noyes 2005).

To search for transit signatures we use an evolution of the box-least-squared (BLS) detection scheme described by Collier Cameron *et al.* (2006). The BLS search covers a period range from 0.35–10.0 d. At present we exclude periods in the ranges 0.53–0.57 d and 0.95–1.05 d, as detections in these period ranges are almost invariably spurious and due to residual instrumental systematic effects. The BLS code is tuned to search for box-like signatures with durations in the range 1.5–3.75 h. We investigate the performance of the latest methods (BLS, AOVTR, etc., see Tingley 2003 for a review) on our data sets, and apply more than one method to identify the most convincing transit candidates.

Once a candidate transit signature is detected by the BLS code, its parameters are further refined using a Markov Chain Monte-Carlo (MCMC) algorithm as described by Collier Cameron *et al.* (2007). The results from the MCMC analyses of the candidate transits are then imported into a database, and subjected to manual filtering, eye-balling and prioritization before being fed into the follow-up programme.

6. QES Follow-Up Strategy

The first stage in the follow-up of convincing transit candidates is to estimate the stellar density and the planetary radius by fitting the transit profiles from the survey data themselves. We use the pre-filtering methodology developed by the WASP Project (Collier Cameron *et al.* 2007) to identify candidate planetary systems. The stellar effective temperature is estimated from the 2MASS $J-H$ color index. This yields an estimate of the stellar mass under the assumption that the star is on the main sequence, and a set of non-linear limb-darkening coefficients as tabulated by Claret (2000). We use the small-planet model of Mandel and Agol (2002) to fit the transit light curve as function of the epoch T_0 of mid-transit, the orbital period P, the total duration t_T from first to fourth contact, the ratio $R_p/R_\star$ of the planetary to the stellar radius, and the impact parameter b of the planet's trajectory across the stellar disk. A Markov-chain Monte Carlo (MCMC) algorithm is used to determine the posterior probability distributions for each of the fitting parameters.

The posterior probability distribution for the planetary radius yields the probability that the planet has a radius less than 1.5 times that of Jupiter. We also determine the departure of the fitted stellar radius from the main-sequence value expected for a star of the catalogued $J-H$ color. As Sozzetti *et al.* (2007) have noted, the stellar density is related in a fundamental and model-independent way to the ratio of the transit duration t_T to the orbital period P. The location of the system in a plot of $R_\star/M_\star^{1/3}$ *vs.* T_{eff} gives a direct assessment of the star's proximity to the main sequence. Many astrophysical false-positive configurations in which an eclipsing stellar binary is blended with a brighter star can be detected and eliminated because the stellar density derived from the transit duration is inconsistent with the effective temperature derived from the $J-H$ color. At this stage we

also fit a cosine curve with half the orbital period to determine the amplitude and significance of any ellipsoidal variation out of transit. Any significant tidal distortion of the primary indicates that the orbiting companion must be of stellar mass, eliminating the system as a planet candidate (Sirko and Paczyński 2003).

For candidates whose transit parameters indicate an object of planet-like radius orbiting a star that appears to be on the main sequence, the next step is to obtain high-accuracy high-cadence light curves covering the suspected transit event, and covering the light curve phase where a secondary eclipse might occur if the system is an eclipsing binary. For the brightness range of our survey target stars, this can be achieved by a 1 m class telescope. Transit candidates are rejected upon the detection of secondary eclipses, ellipsoidal variations, and/or heating effects, all indicative of an eclipsing binary rather than a *bona fide* transiting planet. The higher angular resolution of the 1 m class telescope helps us to resolve cases where the transits originate in a nearby, faint stellar binary located close to a brighter star. Further MCMC analysis of the follow-up transit light curve and host star properties (color, spectral type etc.) yields a minimum radius for the transiting body, which can be used to reject a planetary transit candidate if its value is too large ($> 2R_J$).

For the purpose of follow-up observations, the SuperWASP Alsubai Follow-up Telescope (SAFT) is being constructed as a 1-m robotic telescope facility on La Palma in the Canary Islands. The aim of the telescope is solely for transit candidate follow-up, shared with the SuperWASP Project. The QES Project will access $\approx 35\%$ of the observing time in return for the investment in the construction and running costs. The project has been granted permission to place the telescope at the observatory site, and the construction is in progress. It is estimated to be finished most likely in early 2014.

Candidates that pass the photometric follow-up stage are then placed on candidate lists for radial-velocity measurements. The existing collaborations between WASP Consortium and the Geneva CORALIE team and the French SOPHIE consortium have developed a highly efficient and successful strategy modeled on that described by Pont *et al.* (2005) for Doppler follow-up of OGLE transit candidates. An initial reconnaissance observation is used to screen for extreme rotation (which precludes determination of a planetary orbit) or obvious double-lined spectroscopic binaries. Surviving candidates are re-observed a day or so later, to eliminate single-lined binaries with unseen companions of stellar mass. Subsequent radial velocity observations target the quadrature phases of the orbit, to determine the total radial-velocity amplitude and hence the planetary mass. Further observations are then obtained to determine the radial acceleration near both conjunctions, to estimate the orbital eccentricity. For candidates brighter than $V = 13$ mag or so, we combine our candidate lists with the WASP programmes on CORALIE in the southern hemisphere and SOPHIE in the north. For fainter candidates we will submit our own observing proposals to carry out radial-velocity follow-up using 4–10 m class telescopes.

7.   Initial Results from QES

Figs. 5 and 6 show the RMS of the magnitude residuals for two fields taken with the 200 mm and the 400 mm cameras, respectively. These plots show the residuals before and after being detrended with the SYSREM algorithm. It can be seen from Figs. 5–6 that as planned the 400 mm camera samples a much fainter magnitude range with a good RMS precision. The 200 mm camera is imaging the bright stars and providing an overlap in detection for stars in the *V* magnitude range from 10 to 12. Many QES candidates are discovered independently by both the 200 mm and 400 mm cameras, in the magnitude range where the two systems overlap. This dual detection capability adds confidence that the detected transits are real and not due to systematic errors. The QES data are also producing transiting candidates around much fainter stars, with some $V \approx 15$ mag stars being flagged as candidates.
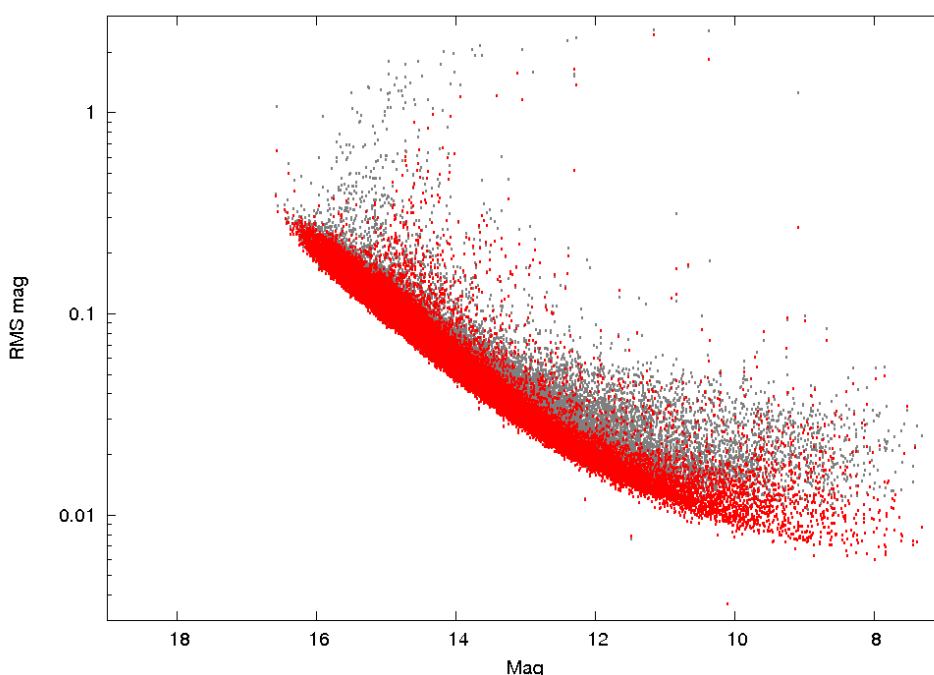

Fig. 5. RMS plot showing the star magnitude residuals for the 200 mm camera for a whole field's worth of data. The RMS scatter is shown before (grey) and after (red) being detrended with the SYSREM algorithm.

QES is also independently identifying a number of transiting exoplanets found first by other surveys such as SuperWASP. Several of these planets were independently flagged as A-list candidates in the QES data before later checks with the SuperWASP database showed them to already be confirmed planets. Figs. 7 and 8 show two such examples. Fig. 7 shows the QES light curve and corresponding periodogram of WASP-37 obtained with one of the 400 mm cameras. The QES
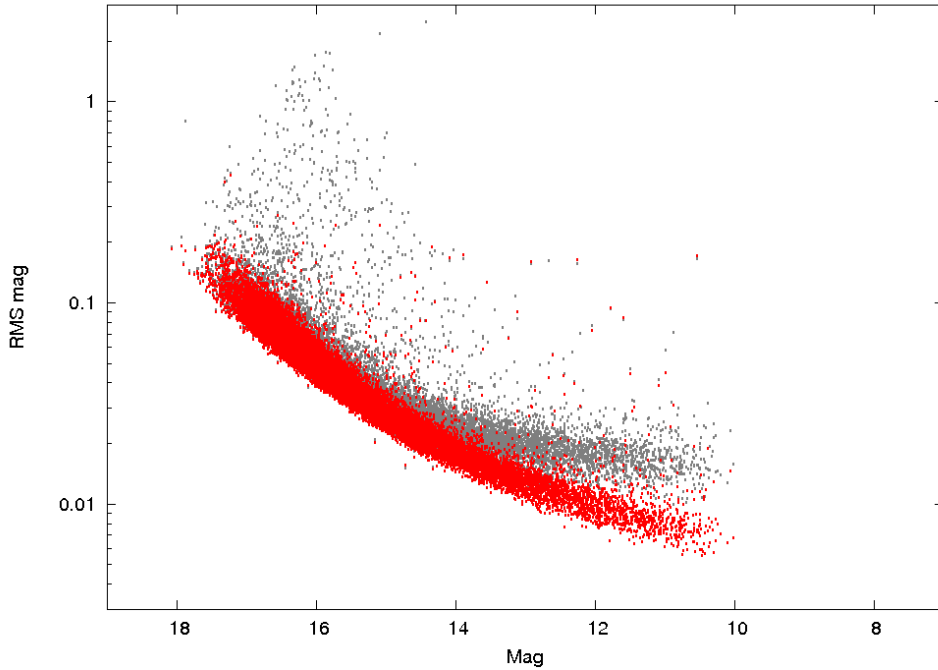
Fig. 6. RMS plot of the star magnitude residuals for one of the 400 mm cameras for a whole field's worth of data. The RMS scatter is shown before (grey) and after (red) being detrended with the SYSREM algorithm.
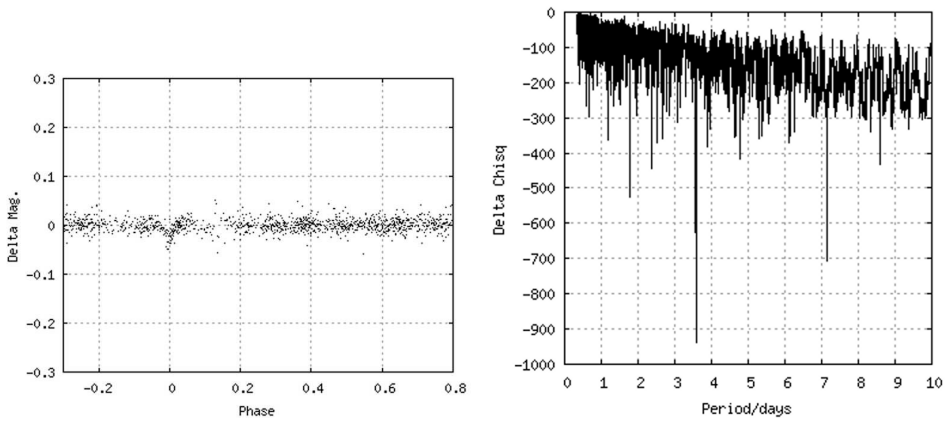

Fig. 7. QES light curve and periodogram of WASP-37b, an exoplanet detected by SuperWASP (Simpson *et al.* 2011) and independently flagged in the QES database.

data reveal the transit signature and the QES periodogram identifies the correct period independently of the SuperWASP data that first found the transits. WASP-37b is a $1.8 M_J$ $1.2 R_J$ planet in a 3.58 d orbit around a $V = 12.7$ mag metal-poor G2 dwarf (Simpson *et al.* 2011). Fig. 8 shows the QES light curve and periodogram for WASP-36. This $V = 12.7$ mag metal-poor G2 dwarf hosts a $1.3 M_J$ $2.3 R_J$ planet
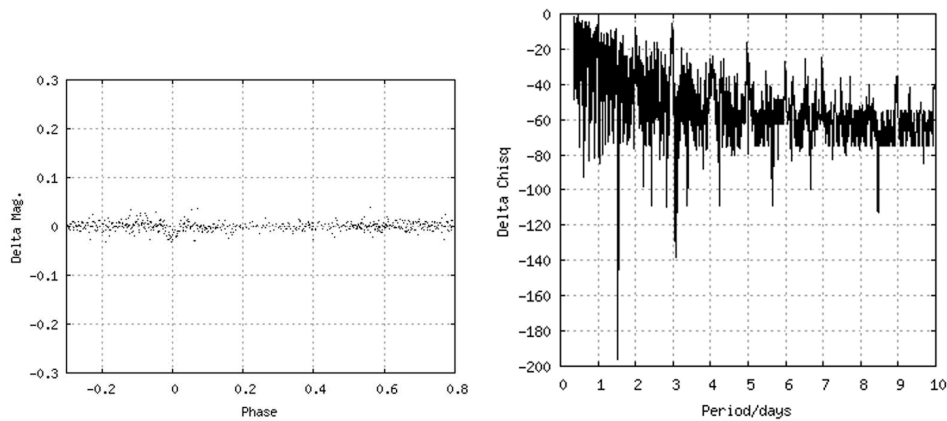
Fig. 8. QES light curve and periodogram of WASP-36b, an exoplanet detected by SuperWASP (Smith *et al.* 2012) and independently flagged in the QES database.

in a 1.54 d orbit (Smith *et al.* 2012). The transit is clearly detected in the QES light curve from one of the 400 mm cameras, and the QES periodogram identifies the correct period.

The QES project has been collecting data since mid November 2009. The first 34 fields that were processed and ingested into the archive yielded 1 863 375 935 photometric data points on a total of 951 417 stars. QES has identified hundreds of promising candidates, dozens of which have been promoted to the A-list for photometric and radial velocity follow up. The first two QES planets, Qatar 1b (Alsubai *et al.* 2011) and Qatar 2b (Bryan *et al.* 2012), have already been confirmed.

The next stage in the development of QES is a planned deployment of similar camera systems at two complementary longitudes in the northern hemisphere. The more nearly continuous temporal coverage afforded by a 3-site survey should greatly reduce the time needed to identify candidates and establish reliable transit ephemerides prior to photometric and radial velocity follow-up observations. Given the quality of the light curves that the QES project is producing and the effective validation of candidate filtering methods, we can anticipate that QES will find many more transiting exoplanets among which will be hot Saturns and hot Neptunes orbiting stars bright enough for follow-up investigations.

REFERENCES

Alsubai, K.A., *et al.* 2011, *MNRAS*, **417**, 709.
Bramich, D.M. 2008, *MNRAS*, **386**, 77.
Bramich, D.M., *et al.* 2013, *MNRAS*, **428**, 2275.

Bryan, M.L., *et al.* 2012, *ApJ*, **750**, 84.

Chabrier, G., Baraffe, I., Leconte, J., Gallardo, J., and Barman, T. 2009, *in: American Institute of Physics Conference Series Ed. E. Stempels*, **1094**, 102.

Charbonneau, D., Brown, T.M., Latham, D.W., and Mayor, M. 2000, *ApJ*, **529**, L45.

Claret, A. 2000, *A&A*, **363**, 1081.

Collier Cameron, A., *et al.* 2006, *MNRAS*, **373**, 799.

Collier Cameron, A., *et al.* 2007, *MNRAS*, **380**, 1230.

Dong, S., and Zhu, Z. 2013, *ApJ*, **778**, 53.

Henry, G.W., Marcy, G.W., Butler, R.P., and Vogt, S.S. 2000, *ApJ*, **529**, L41.

Horne, K. 2003, *in: Astronomical Society of the Pacific Conference Series – Scientific Frontiers in Research on Extrasolar Planets, Ed. D. Deming and S. Seager*, **294**, 361.

Ida, S., and Lin, D.N.C. 2004, *BAAS*, **36**, 850.

Kovács, G., Bakos, G., and Noyes, R.W. 2005, *MNRAS*, **356**, 557.

Liu, X., Burrows, A., and Ibgui, L. 2008, *ApJ*, **687**, 1191.

Mandel, K., and Agol, E. 2002, *ApJ*, **580**, L171.

Mayor, M., and Queloz, D. 1995, *Nature*, **378**, 355.

Mazeh, T., *et al.* 2000, *ApJ*, **532**, L55.

Perryman, M.A.C. 2000, *Reports on Progress in Physics*, **63**, 1209.

Pollacco, D.L., *et al.* 2006, *PASP*, **118**, 1407.

Pont, F.,Bouchy, F., Melo, C., Santos, N.C., Mayor, M., Queloz, D., and Udry, S. 2005, *A&A*, **438**, 1123.

Simpson, E.K., *et al.* 2011, *AJ*, **141**, 8.

Sirko, E., and Paczyński, B. 2003, *ApJ*, **592**, 1217.

Smith, A.M.S., *et al.* 2012, *AJ*, **143**, 81.

Sozzetti A., *et al.* 2007, *ApJ*, **664**, 1190.

Tamuz, O., Mazeh, T., and Zucker, S. 2005, *MNRAS*, **356**, 1466.

Tingley, B. 2003, *A&A*, **408**, 5.

Udalski A., *et al.* 2002, *Acta Astron.*, **52**, 1.

Zacharias N., *et al.* 2010, *AJ*, **139**, 2184.